

# Beam Test of Silicon Strip Sensors for the ZEUS Micro Vertex Detector

L.A.T. Bauerdick <sup>1(a)</sup>, E. Borsato <sup>2</sup>, C. Burgard <sup>1</sup>, T. Carli <sup>1</sup>, R. Carlin <sup>2</sup>,  
M. Casaro <sup>2</sup>, V. Chiochia <sup>1</sup>, F. Dal Corso <sup>2</sup>, D. Dannheim <sup>1</sup>, A. Garfagnini <sup>5(b)</sup>,  
A. Kappes <sup>3</sup>, R. Klanner <sup>5</sup>, E. Koffeman <sup>4</sup>, B. Koppitz <sup>5</sup>, U. Kötzt <sup>1</sup>, E. Maddox <sup>4</sup>,  
M. Milite <sup>1(c)\*</sup>, M. Moritz <sup>1</sup>, J.S.T. Ng <sup>1(d)</sup>, M.C. Petrucci <sup>1</sup>, I. Redondo <sup>6(e)\*</sup>,  
J. Rautenberg <sup>3(f)</sup>, H. Tiecke <sup>4</sup>, M. Turcato <sup>2</sup>, J.J. Velthuis <sup>4</sup>, A. Weber <sup>3</sup>

- (1) Deutsches Elektronen-Synchrotron DESY, Hamburg, Germany
- (2) Dipartimento di Fisica dell' Università and INFN, Padova, Italy
- (3) Physikalisches Institut der Universität Bonn, Bonn, Germany
- (4) NIKHEF and University of Amsterdam, Amsterdam, Netherlands
- (5) Hamburg University, Institute of Exp. Physics, Hamburg, Germany
- (6) Universidad Autonoma de Madrid, Madrid, Spain
- (a) Now at Fermi National Accelerator Laboratory FNAL, Batavia, Illinois, USA
- (b) Now at Dipartimento di Fisica dell' Università and INFN, Padova, Italy
- (c) Now at Hamburg University, Institute of Exp. Physics, Hamburg, Germany
- (d) Now at the Stanford Linear Accelerator Center SLAC, Stanford, California, USA
- (e) Now at Laboratoire Leprince Ringuet - Ecole Polytechnique, Route de Saclay 91128 Palaiseau Cedex, France
- (f) Supported by the GIF, contract I-523-13.7/97.

\* Corresponding authors. Tel: +33 1 69 33 44 05 ; fax:+33 1 69 33 30 02

*E-mail addresses* : redondo@poly.in2p3.fr (I. Redondo), milite@mail.desy.de (M. Milite).

---

**Abstract**

For the HERA upgrade, the ZEUS experiment has designed and installed a high precision Micro Vertex Detector (MVD) using single sided  $\mu$ -strip sensors with capacitive charge division. The sensors have a readout pitch of 120  $\mu\text{m}$ , with five intermediate strips (20  $\mu\text{m}$  strip pitch). An extensive test program has been carried out at the DESY-II testbeam facility. In this paper we describe the setup developed to test the ZEUS MVD sensors and the results obtained on both irradiated and non-irradiated single sided  $\mu$ -strip detectors with rectangular and trapezoidal geometries. The performances of the sensors coupled to the readout electronics (HELIX chip, version 2.2) have been studied in detail, achieving a good description by a Monte Carlo simulation. Measurements of the position resolution as a function of the angle of incidence are presented, focusing in particular on the comparison between standard and newly developed reconstruction algorithms.

*PACS* : 29.40.Gx; 29.40.Wk; 07.05.kj

*Keywords* : ZEUS; Beam test; Silicon; Microstrip; Position reconstruction algorithms

---

## 1 Introduction

The HERA  $ep$  collider luminosity upgrade [1] performed during the years 2000-2001 aims to increase the instantaneous luminosity from 1.5 to  $6 \cdot 10^{31} \text{ cm}^{-2} \text{ s}^{-1}$ , providing thus a higher sensitivity to low cross section physics. The ZEUS experiment [2] has been equipped with a new silicon Micro Vertex Detector (MVD) which is going to improve the global precision of the existing tracking system, allowing to identify events with secondary vertices coming from the decay of long-lived states such as hadrons with charm or bottom and  $\tau$  leptons. Moreover, the detector acceptance will be enhanced in the forward region,

along the proton beam direction, improving for example the detection of very high  $Q^2$  scattered electrons and the reconstruction of the interaction vertex in high  $x$  charged current events<sup>1</sup>.

According to the design specifications [3,4,5,6], the MVD is composed of a barrel (BMVD) and forward (FMVD) part, requiring a good matching with the existing detectors. The MVD had to fit inside a cylinder of 324 mm diameter defined by the inner wall of the Central Tracking Detector (CTD). The readout electronics, based on the HELIX chip (version 3.0) [7,8] is mounted inside the active area, close to the silicon diodes. The silicon sensors are single sided, AC coupled, strip detectors with capacitive charge division; the readout pitch is 120  $\mu\text{m}$  and the strip pitch is 20  $\mu\text{m}$ . A sketch of the silicon sensor can be seen in figure 1. The BMVD (FMVD-1,FMVD-2) sensors have a rectangular (trapezoidal) geometry with 6.4 cm x 6.4 cm (base=6.4 cm  $\times$  height=7.35 cm and 6.4 cm  $\times$  4.85 cm, respectively) dimensions. In the FMVD, the sides of the trapezoid are tilted by  $180^\circ/14$  with respect to the bases and the strips are parallel to one of the tilted sides of the trapezoid, having thus different lengths across the sensor. The biasing of the strips is implemented using polysilicon resistors ( $\sim 1.5\text{-}2.5\text{ M}\Omega$ ) connected to the sensor ground line (called in the following biasing ring), located alternatively on both ends of the strips. The first and last strips close the biasing ring, being directly connected to it. Three  $\text{p}^+$  guard rings, designed to adjust the potential towards the detector edges, surround the sensitive area. An additional  $\text{n}^+$  doped implant beyond the last guard ring allows to bias the backplane with a contact from the top. Detailed descriptions of the MVD design and mechanical structure can be found in [5,9,10,11]. The detailed design of the silicon sensors and results on

<sup>1</sup>  $-\overline{Q^2}$  is the exchanged photon invariant mass;  $x$  is the fraction of the proton momentum carried by the struck quark.

the electrical measurements are described elsewhere [12, 13, 14].

The testbeam program for the MVD had several goals:

- to study the general performance of sensors with minimum ionising particles (i.e. noise level, pedestal stability, hit efficiency, charge division);
- to test prototype versions of frontend electronics (i.e. readout chips and hybrids) ;
- to test the sensors at different bias voltages;
- to measure the position resolution for different angles of incidence in order to optimise reconstruction algorithms;
- to study the effect of irradiation.

The data have been compared with the results of a Monte Carlo program for the silicon sensor simulation in order to gain input for the vertex detector simulation. The detector performances have been studied using three non-irradiated and two additional irradiated sensors [15, 14]. A barrel sensor was irradiated using photons from a  $^{60}\text{Co}$  source: the detector was left floating and irradiated up to an integrated dose of 2.0 kGy. A second sensor was irradiated with reactor neutrons having a fluency  $\phi_e = 10^{13} \text{ 1 MeV}_{\text{equiv. n/cm}^2}$ . No substantial effects due to radiation damage on the detector performances have been observed. All results presented in the following sections refer to non-irradiated sensors and to the sensor irradiated floating with 2 kGy of  $^{60}\text{Co}$  photons.

After a brief description of the testbeam setup in section 2, the treatment of the data and the general performance of the detectors are summarised in section 3. The detector simulation is described in section 4. Section 5 is devoted to studies which use perpendicular tracks. It also describes the extraction of the intrinsic position resolution. The position resolution as a

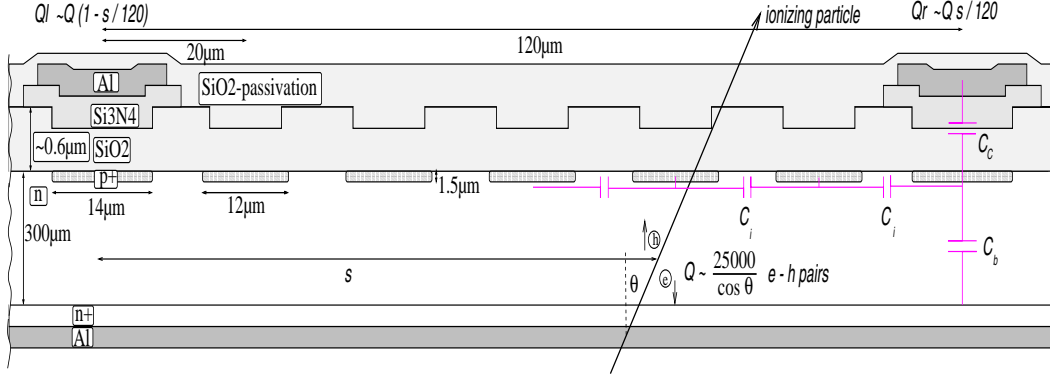


Fig. 1. Cross section of a MVD silicon sensor between two readout strips (drawing not to scale). Dimensions of the layers are given in the left part of the picture. On the right side a simplified picture of the capacitive network is shown.

function of the angle of incidence is studied in detail in sections 6 and 7. The paper ends with a summary of the results.

## 2 Test beam setup

The measurements were performed at the DESY-II testbeam, a parasitic electron beam obtained after two conversions: a  $10 \mu\text{m}$  thick carbon-fiber target in the machine intercepts the beam and produces bremsstrahlung photons which are converted into electron-positron pairs in a  $0.1 X_0$  thick copper target. A bending magnet together with a momentum defining collimator slit delivers the beam into the experimental hall. Depending on the primary use of DESY-II the maximal momentum varies between 4.3 and 7.5 GeV/c. Most measurements were done at 3 and 6 GeV/c resulting in a trigger rate of  $\sim 10$  Hz and  $\sim 2$  Hz, respectively.

A silicon reference telescope has been assembled to allow a precise determination of the particle impact point on the detector to be studied. Both, the telescope modules and the module holding the MVD detector are mounted

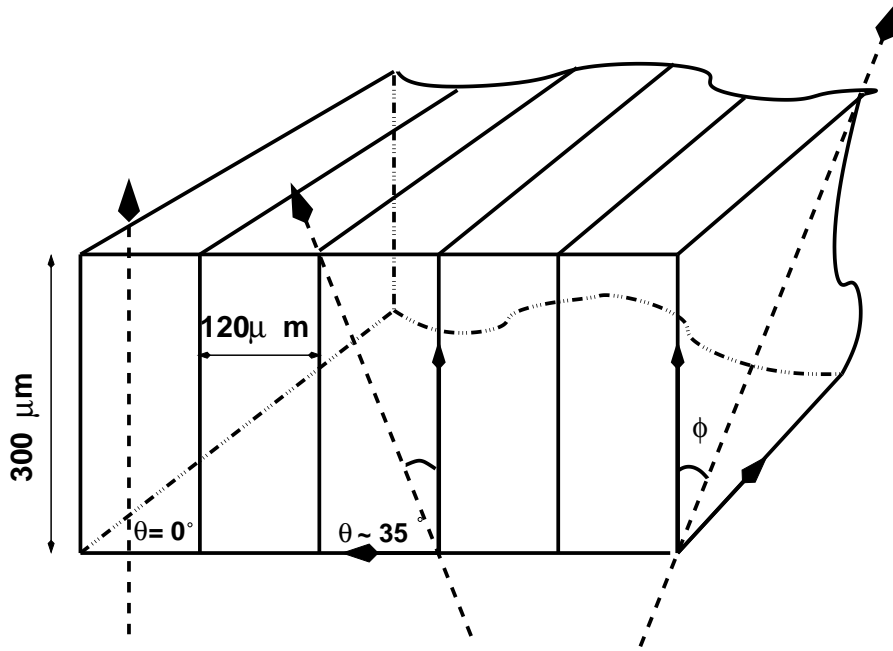


Fig. 2. Schematic cross section of a MVD silicon sensor to scale. The angles of incidence  $\theta$  and  $\phi$  are indicated.

on a common optical bench. The detector to be studied is mounted between the telescope modules on linear and rotational positioners which allow to investigate the performance in different areas of the detector and for different angles of incidence. The rotations can be around the strip axis ( $\theta$  angle) or around the axis perpendicular to the strip in the detector plane ( $\phi$  angle) (see figure 2). A trigger was generated by coincidence of the signals from scintillator fingers located at both end sides of the optical bench. A drawing of the testbeam setup is shown in figure 3. The data acquisition system is based on an embedded Sun workstation in a VME-crate which controls the initialisation of the readout modules, the readout chips, the pattern generators, the GPIB-interface for the positioners and the data taking. The system is run under LabView [16].

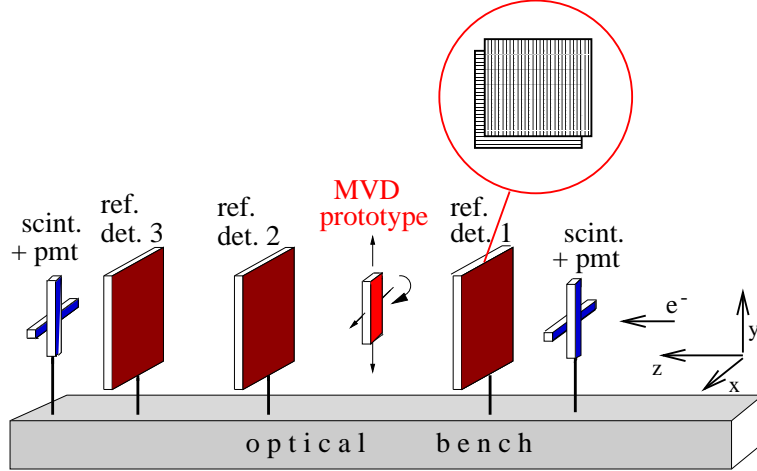


Fig. 3. Schematic drawing of the testbeam setup.

### 2.1 Beam telescope

The beam telescope consists of 3 modules which define the track in two coordinates along the telescope. The modules are a version of a CERN development described in [17,18]. They consist of two  $300\ \mu\text{m}$  thick single-sided silicon detectors of  $32 \times 32\ \text{mm}^2$  size with a strip pitch of  $25\ \mu\text{m}$  and a readout pitch of  $50\ \mu\text{m}$ ; the strip direction of the detectors are perpendicular to each other.

All detectors have a very good S/N (i.e. signal over noise ratio for minimum ionising particles)<sup>2</sup>,  $80 < S/N < 130$ , and a low fraction of dead channels and noisy strips ( $< 0.1\%$ ). The extrapolation to infinite momentum results in an intrinsic resolution of  $2.8 \pm 0.1\ \mu\text{m}$  (in section 5 the analysis method applied to determine the intrinsic resolution of a silicon detector is discussed).

The MVD detector is aligned with respect to the closest reference detectors (1 and 2). The achieved precision of the alignment procedure [19] is  $< 1\ \mu\text{m}$ .

<sup>2</sup> The term noise (N) refers to the single strip noise.

## 2.2 MVD detector readout

The MVD detectors were operated in the test beam using prototype versions of the HELIX readout chip (version 2.2), developed for the Hera-B experiment [7, 8]. The HELIX chip provides 128 analog channels with a charge sensitive pre-amplifier and shaper, forming a semi-Gaussian pulse with a peaking time of  $\sim 50\text{-}70$  ns. The signals are sampled in an analog pipeline capable of storing 128 events with 8 extra channels for trigger derandomisation. The chip can be operated up to 40 MHz clock-rate. In the ZEUS experiment it will be used at 10 MHz write and read speed. In order to simplify the readout system in the testbeam, it was decided to synchronise the chip clock to the synchrotron revolution frequency of about 1.05 MHz; with this setting particles traversing the detectors were in a fixed phase relation to the chip clock. Tests performed using a frequency multiplier of 10 (which are not discussed in the present paper) showed no difference in the detector performances.

## 2.3 MVD detector assembly

In the testbeam, a protection circuit, including a protection resistance of  $0.5\text{ M}\Omega$ , was introduced between the backplane contact and the power supply. In the following, the voltage applied between the biasing ring and the backplane is referred to as  $V_{bias}$ . The detectors were biased at full depletion, unless otherwise stated. The Barrel and Forward MVD detectors are connected to the front-end electronics using a Upilex [20] “fan-out” foil with conductive lines. The Upilex circuits are made of an Upilex S substrate, a  $50\text{ }\mu\text{m}$  thick polyimide film. A conductive layer of  $5\text{ }\mu\text{m}$  electro-plated copper is deposited on top and separated from the substrate by means of a  $150\text{ nm}$  thick nickel adhesion layer. A  $1.5\text{ }\mu\text{m}$  gold layer is deposited over the conductive strips and the pads



used for bonding. The Upilex circuits for the Barrel and Forward modules are produced at CERN [21]. The strip pitch is  $120\ \mu\text{m}$  on the detector side and is reduced to  $100\ \mu\text{m}$  on the hybrid, where the Upilex strips are connected to a pitch adapter which further reduces the readout pitch to  $41.4\ \mu\text{m}$  of the HELIX input bond pads. The front-end electronic is mounted on a multi-layer Hybrid structure ( $40 \times 70\ \text{cm}^2$ ) supporting 4 HELIX chips which are needed to read-out the 512 strips of a BMVD detector; for the FMVD detector only 480 readout channels are required.

### 3 Data analysis and general performance

The digitised ADC output coming from the MVD detector and the telescope detectors is stored in files during the data taking. The channel noise and pedestal levels are measured using special random trigger runs of 100-200 events taken without beam. In order to reduce the data volume, for the telescope data, zero suppression is performed directly in the CAEN V550 ADC, using a threshold level of 3 times the channel noise. No selection is applied to the raw data for the MVD detector.

During the offline analysis, the common mode noise (CMN) and the pedestal levels are subtracted from the data [19]. The pedestal, determined once per day, has shown negligible variation over time. The variation of the pedestals within one readout chip, from the first to the last readout channel, has been found to be of the order of the cluster pulse height. The strip noise was stable and showed uniform behaviour; its variation within regions read by the same chip are much smaller than those observed between chips ( $\sim 20\%$ ). No dependence of the noise on the strip length (varying between 6 mm and 73.3 mm) was observed [22]. The common mode noise is Gaussian distributed with

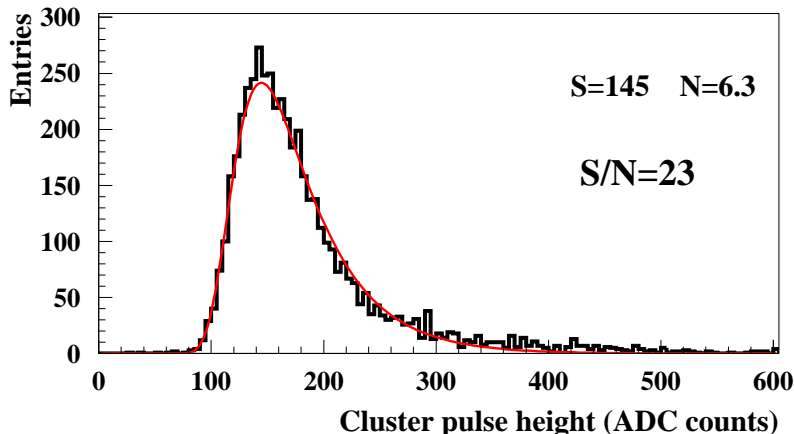


Fig. 4. Two strip cluster pulse height distribution. A Landau fit is superimposed to the data; the following parameterisation has been used:  $p_1 \exp[-0.5 \cdot (\lambda + \exp(-\lambda))]$  where  $\lambda = p_3(x - p_2)$ , and  $p_1$ ,  $p_2$  and  $p_3$  are free parameters of the fit.

a rms comparable to the single strip noise level.

A cluster seed is identified by looking for the highest signal strip in the detector. All neighbouring strips with a signal larger than a certain threshold level  $T$  (usually  $T = 3 \times \sigma_{\text{chip}}$ , where  $\sigma_{\text{chip}}$  is the average chip noise) are added to form a cluster. The cluster pulse height and size are then defined as the sum of the signals from all the strips and the total number of strips belonging to the cluster, respectively.

For the determination of the S/N using perpendicular tracks, only the strip with the highest signal and its neighbouring strip (left or right) with the higher pulse height are selected and the sum of their pulses defines in this case the total cluster signal. Figure 4 shows the resulting cluster pulse height distribution: the data are fitted by a Landau function. A S/N between 20 and 24 has been obtained for different detectors and readout chips.

An asymmetric cross talk has been observed in the HELIX readout chip: measurements with an external test pulse have shown that when pulsing a channel, a fraction of the input charge is found on the previous (next) channel for even (odd) channels [23]. Using testbeam data, the asymmetric cross talk has been determined to be around 5% for all chips [19]. The cause of this effect is presumably due to an asymmetry in the chip pipeline design. All testbeam data are corrected for asymmetric cross talk.

### 3.1 Gain calibration

The whole detector was illuminated in order to study the uniformity in gain of the channels in terms of the relative calibration constants,  $\text{cal}(i)$ :

$$\text{cal}(i) = \frac{\langle \Sigma \rangle_{\text{channels}}}{\Sigma(i)} \quad \text{with} \quad \Sigma(i) = \overline{S_{\text{max}-1}}^{\text{hit}}(i) + \overline{S_{\text{max}}}^{\text{hit}}(i) + \overline{S_{\text{max}+1}}^{\text{hit}}(i) \quad (1)$$

where  $i$  is the channel number;  $\langle \rangle_{\text{channels}}$  is an average over channels ;  $\overline{S}^{\text{hit}}$  averages over hits;  $S_{\text{max}}$  is the charge of the strip with the maximum charge of the event and  $S_{\text{max}\pm 1}$  is the charge of the strip with position  $\# \text{maximum} \pm 1$ . The gain for all channels of a BMVD and a FMVD-1 detector are shown in figure 5. The mean gain value and the rms of each chip are given in table 1. The first and the last strip (which have only one neighbour) as well as all the broken strips and their direct neighbour strips are excluded and their calibration constants are set to zero in the calibration procedure. The differences of the strip gains for one chip are smaller than 2% and comparable with the statistical uncertainty on the gain calibration ( $\sim 1\%$ ); the calibration constants differ from chip to chip by up to 20 %.

A possible dependence of the gain on the strip length has been investigated since it could introduce left-right asymmetries affecting the position recon-

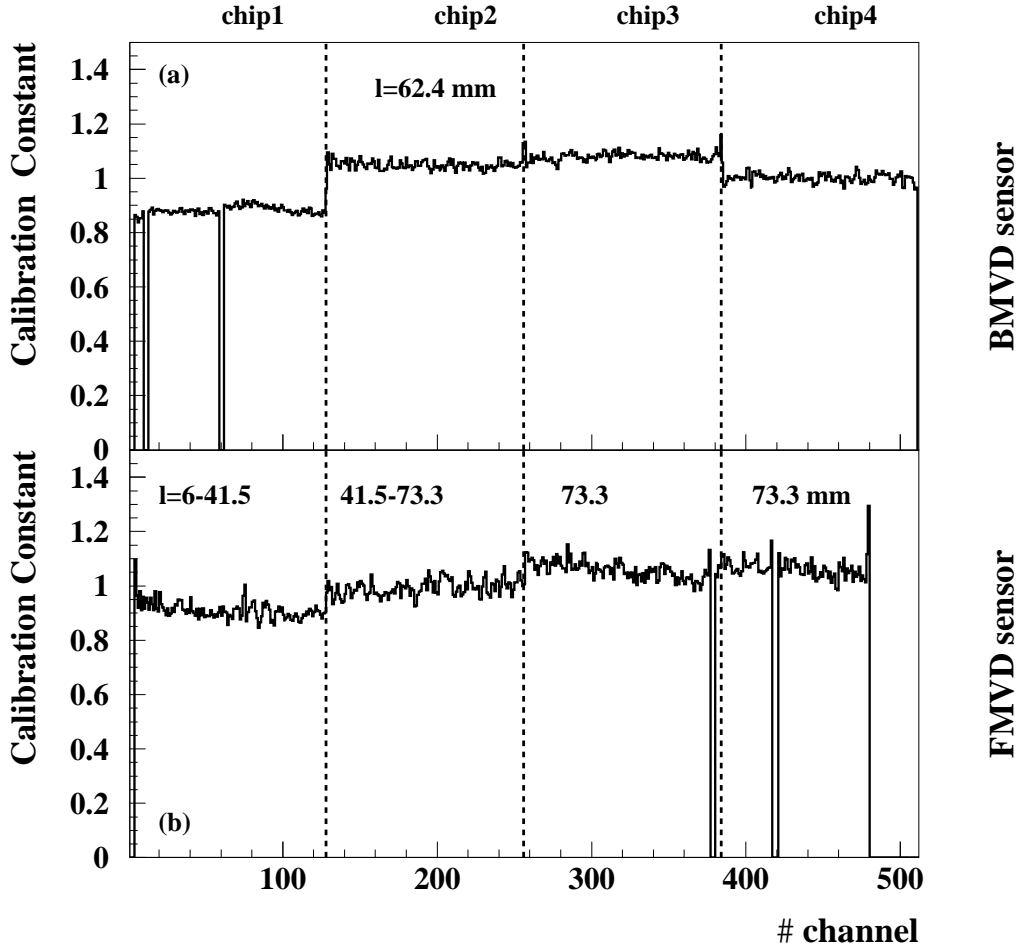


Fig. 5. Calibration constants for 512 channels of one BMVD detector (a) and 480 of a FMVD-1 detector (b) readout by four HELIX chips each. The strip regions read out by different chips are separated by the dashed vertical lines. “l” is the strip length range for one chip region.

struction algorithms. The rms of the calibration constants for strips within a chip of a FMVD-1 detector (table 1, right) are comparable to the statistical uncertainty (2-3 %). The mean of the calibration constants and the S/N within a chip follow the same pattern: regions 3 and 4 (long and constant length strips) have smaller signal than region 1 and 2 (short and variable length strips). No correlation between the calibration constants and the strip

Table 1

S/N, mean and rms of the calibration constants in regions read out by the same chip for a BMVD and FMVD-1 detectors.

	BMVD detector				FMVD-1 detector			
	chip 1	chip 2	chip 3	chip 4	chip 1	chip 2	chip 3	chip 4
length (mm)	62.4	62.4	62.4	62.4	6-41.5	41.5-73.3	73.3	73.3
Mean	0.884	1.050	1.081	1.001	0.909	0.990	1.062	1.070
Rms	0.016	0.017	0.016	0.017	0.036	0.024	0.029	0.039
S/N	20.8	21.9	21.4	21.2	24.7	23.6	21.0	20.7

number (and therefore the strip length) is observed. Since the relative gain is constant for a readout chip, no calibration has been applied in the analyses presented in this paper<sup>3</sup>.

### 3.2 Hit efficiency

The hit efficiency is defined as

$$\epsilon = N_{\text{events}}(\text{Hit})/N_{\text{events}}^{\text{triggered}} \quad (2)$$

where ‘‘Hit’’ is equivalent to the presence of 1 strip with signal larger than  $n$  times the noise ( $n=5,3$ ) in a region of 2.4 mm centred on the position predicted by the telescope. The particle impact position was reconstructed using two reference detectors; in order to avoid contamination from double tracks, only events with a single cluster in all planes of the two telescope modules were

<sup>3</sup> The scintillator fingers used for triggering define a surface of 9 mm  $\times$  9 mm which is well within the detector area readout by a single HELIX chip.

accepted.

Using a sample of  $\sim 10^5$  events the 90% confidence limits on  $\epsilon$  is 99.96%  $>$   $\epsilon_5 > 99.95\%$  (99.997%) for a signal in the MVD detector larger than 5 (3) times the noise.

### 3.3 Detector performance as a function of the bias voltage

The dependence of the detector performance as a function of  $V_{bias}$  has been investigated. Figure 6(a) shows the most probable value of the energy loss distribution<sup>4</sup> and the hit efficiency as a function of the bias voltage. For values of  $V_{bias}$  above the depletion voltage ( $V_{dep} \simeq 85V$ ) a plateau is reached. The signal collection degrades with decreasing  $V_{bias}$ , whereas the hit efficiency remains constant at  $V_{bias}$  well below the depletion voltage. Only for  $V_{bias} \lesssim 40$  V  $\epsilon$  starts to decline. The noise level remains constant ( $\sim 6$  ADC counts) for values of  $V_{bias} > 5V$ .

The charge division of the detector and the position resolution (see sections 3.4 and 5, respectively, for detailed explanations) were also studied as a function of  $V_{bias}$ . Figure 6(b) shows the position resolution as a function of  $V_{bias}$ : a stable behaviour above  $\sim 40$  V can be observed. The charge division of the detector has also found to be unvaried above  $\sim 40$  V [22]. It is remarkable that with  $\sim 9$  V of effective voltage in the detector, with only  $\sim 30\%$  of the bulk depleted, a resolution of  $25 \mu m$  is achieved. As a conclusion, the performance of the detector seems to be rather stable well below depletion voltage.

---

<sup>4</sup> The most probable value of the energy loss distribution is defined as the peak value from a fit by a Landau function.

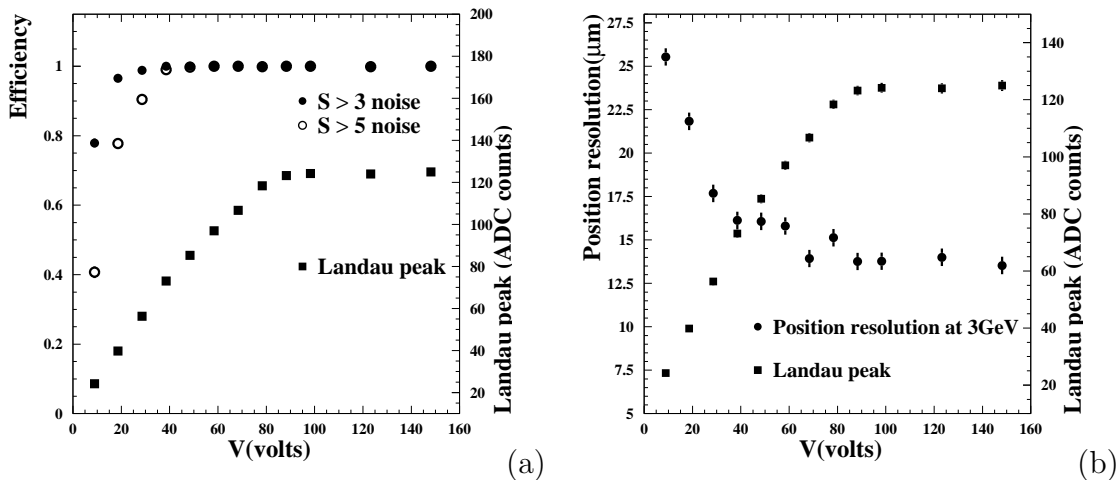


Fig. 6. (a) Most probable value of the energy loss distribution (squares) and hit efficiency (dots) as a function of the bias voltage; (b) position resolution (dots) as a function of the bias voltage.

### 3.4 Charge division

The charge division of the MVD sensors with five intermediate strips was studied using tracks perpendicular to the detector plane.

The charge collected at the strips close to the particle incident position is shown in figure 7. The two readout strips closest to the particle incident position and the next neighbours are labeled strips l (left), r (right), nl (next left) and nr (next right). The most probable value of the charge (obtained by fitting the distribution to a Landau curve) collected by strip l alone and by the sum of strips l and r (l+r) are plotted in bins of the interstrip impact position predicted by the telescope. The normalization factor of all distributions, denoted  $S_{l+r}^{\text{max}}$ , is determined as the sum of the signals detected on strip l and r when a particle crosses the detector exactly underneath a readout strip. When a particle crosses the detector between two readout strips (l and r) the charge collected on the intermediate strips induces charges on the read-

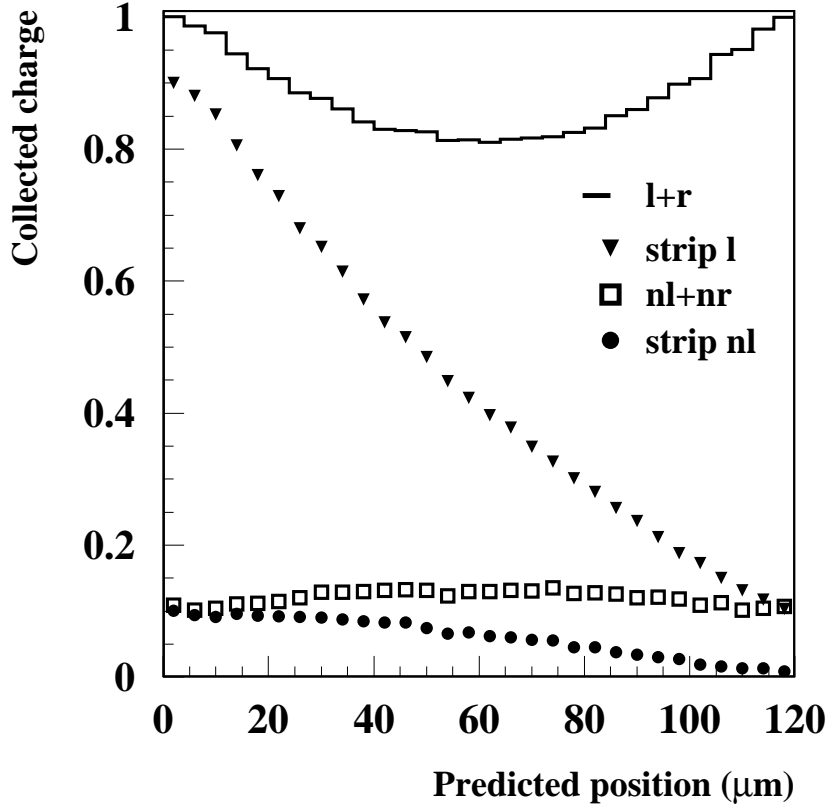


Fig. 7. Sum of the charge collected by the left and right readout strips (sum  $l+r$ , solid line), the charge collected by the left readout strip (strip  $l$ , triangles) falling from the interstrip impact position  $x=0 \mu\text{m}$  to the interstrip impact position  $x=120 \mu\text{m}$ , charge collected by the next left neighbour of the left readout strip (strip  $nl$ , dots) and sum of the charge collected by both the next-to-closest readout strips (sum  $nl+nr$ , open squares).

out ones producing a dependence on the distance to the impact position with large deviations from linearity near the readout strips. Due to capacitive couplings between the strip implants, the fraction of charge collected by strip  $r$  is not negligible ( $\sim 10\% S_{l+r}^{\text{max}}$ ) even for the case of particles crossing the detector exactly underneath the readout strip  $l$  (positions  $x=0$  in figure 7) and vice versa. The charge collected by the next left neighbour of the readout



strip l, nl, and the sum (nl+nr) of the signal collected by the two neighbours to the closest readout strips l (nl) and r (nr) is also shown in figure 7. The measurement demonstrates that a simple model considering only capacitances to neighbouring strip implants resulting in charge collected only at the two neighbour strips is not satisfactory. Moreover, the sum of the two signals collected by strip l and r is not completely flat as a function of the interstrip position, showing a dip (-19 %  $S_{l+r}^{\max}$ ) when the particles cross the detector in the central region between the two readout strips. This is mainly due to charge losses to the backplane. Taking into account the charge sharing to the next-to-closest readout strips, the effective charge loss to the backplane is of the order of  $\sim 16\%$ .

#### 4 Simulation of the MVD detector response

Diffusion, ionisation fluctuations, noise and charge division were included in the simulation program which is described in [24], and is based on [25]. Charge is generated inside the detector along the particle's path implementing ionisation fluctuations tuned to other measurements with silicon detectors [25]. The charge drifts to the detector surface under the effect of the electric field; it is then assumed to be collected by the closest strip implant [25].

Once the charges are collected on the strip implants they have to be transferred to the readout strips. The capacitive network is more complicated than the simple sketch in figure 1, since also capacitances to next to strip implants even further apart are taken into account [26]. Charge transfer coefficients have been determined from testbeam measurements. They give the fraction of charge on a strip implant which is transferred to the surrounding readout strips. To measure these coefficients only tracks crossing the detector within  $5\mu\text{m}$

Table 2

Charge fraction collected by the four readout strips surrounding the particle impact position. Only particles crossing the detector (between strips l and r) directly underneath strip implants are selected.

Particle Position	Charge transfer coefficient				sum
	nl	l	r	nr	
#1: strip l	0.091	0.815	0.091	0.004	1.000
#2: 1 <sup>st</sup> intermediate	0.082	0.655	0.158	0.021	0.916
#3: 2 <sup>nd</sup> intermediate	0.076	0.486	0.256	0.041	0.859
#4: 3 <sup>rd</sup> intermediate	0.058	0.363	0.363	0.058	0.842
#5: 4 <sup>th</sup> intermediate	0.041	0.256	0.486	0.076	0.859
#6: 5 <sup>th</sup> intermediate	0.021	0.158	0.655	0.082	0.916
#7: strip r	0.004	0.091	0.815	0.091	1.000

underneath strip implants were used. The strip implants are numbered from #1 to #7, starting from the left readout strip from the impact position. The charge collected (i.e. the most probable value of the energy loss distribution) on the four surrounding readout strips, denoted as next left (nl), left (l), right (r) and next right (nr), is measured for tracks in positions #1 to #7. High statistics data samples have been used in order to achieve an accuracy better than 1%. The collected charge reaches a maximum for positions #1 and #7; all coefficients are normalized to this value. The detector response is assumed to be symmetric. In the simulation all charges collected on a strip implant are transferred to the four surrounding readout strips using these measured coefficients (fractions smaller than 0.4% were neglected). For every readout channel an additional signal according to Gaussian distributed noise

was simulated. The width of the Gaussian was chosen in order to obtain the same S/N as measured in the testbeam data.

Comparison between the results of the simulation program with the data measurements is presented in section 7.2.

## 5 Position reconstruction for perpendicular tracks

### 5.1 The eta algorithm.

A standard method to reconstruct the impact position, proven to work at small incidence angle, is the so called  $\eta$  algorithm [27], [28]. It consists of a non-linear interpolation between the two neighbouring strips of the cluster which have collected the highest signals (indicated in the following as  $S_{\text{right}}$  and  $S_{\text{left}}$ , respectively). For each event, the quantity  $\eta$ :

$$\eta = \frac{S_{\text{right}}}{S_{\text{right}} + S_{\text{left}}} \quad (3)$$

is calculated. Figure 8 shows the  $dN/d\eta$  distribution for the MVD detector obtained from the testbeam data: in the region close to the readout strips there are very few entries, and clear peaks can be seen elsewhere. In case of a fully linear behaviour, the  $\eta$  distribution would be completely flat and the dashed bands (where the peaks are observed) would represent the position of the intermediate strips. The fact that the  $dN/d\eta$  is not uniform, although the beam profile is uniform over the detector area, indicates that the capacitive charge division mechanism is not fully linear in the hit position between readout strips. To correct for this non-linearities a probability density function (an

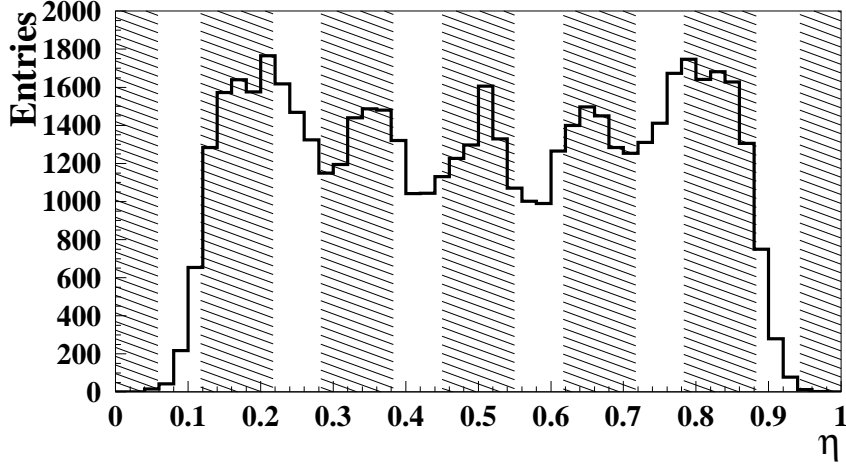


Fig. 8. Example of  $dN/d\eta$  distribution. The dashed area covers the position of the  $p^+$  implants (a linear dependence of  $\eta$  on the interstrip hit position is assumed). example is shown in figure 13) is determined from the data:

$$f(\eta_0) = \frac{1}{N} \cdot \int_0^{\eta_0} \frac{dN}{d\eta} d\eta \quad (4)$$

where  $N$  is the total number of entries in the  $dN/d\eta$  distribution and  $\eta_0$  is the  $\eta$  value for the considered event. The corrected impact position is then given by:

$$y_{\text{rec}} = p \cdot f(\eta_0) + y_{\text{left}} \quad (5)$$

where  $p$  is the readout pitch of  $120 \mu\text{m}$  and  $y_{\text{left}}$  denotes the position of the left strip.

## 5.2 Intrinsic resolution

The intrinsic resolution is defined as the spatial precision of the MVD detector

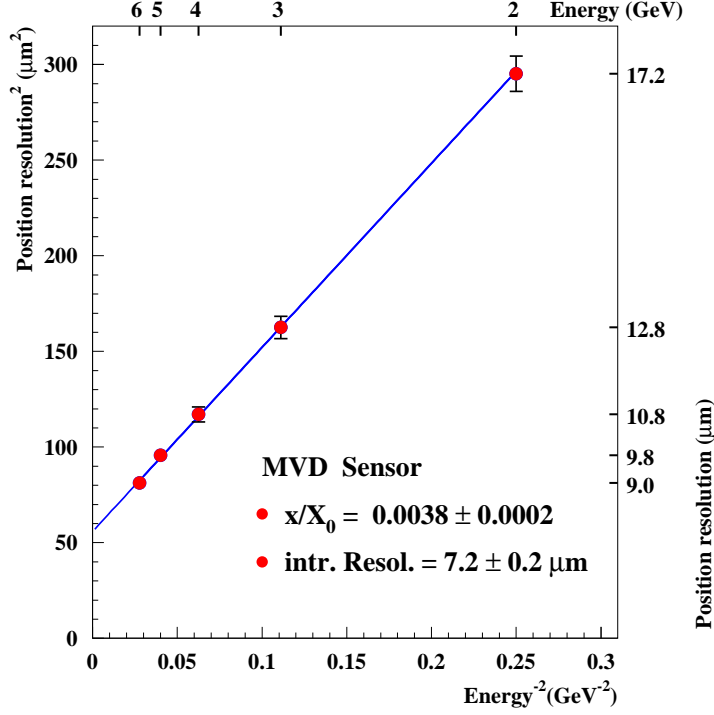


Fig. 9. Position resolution as a function of the beam energy. The result of the fit for the ratio  $x/X_0$  (where  $x$  is the thickness of the material and  $X_0$  the radiation length) is also shown.

The measured position resolution  $\sigma_{\text{res}}$ , defined as the width of the residual distribution obtained from a fit to a Gaussian function, includes several contributions:

$$\sigma_{\text{res}} = \sqrt{(\sigma_{\text{MVD}}^{\text{intr}})^2 + k \cdot (\sigma_{\text{tele}}^{\text{intr}})^2 + \sum_i k_i \cdot \Delta\theta_{\text{ms}}^2} \quad (6)$$

where  $\sigma_{\text{MVD}}^{\text{intr}}$  is the intrinsic resolution of the MVD detector,  $\sigma_{\text{tele}}^{\text{intr}}$  is the intrinsic resolution of the telescope sensors,  $(k, k_i)$  are geometrical factors [24] related to the relative distances between the telescope modules, the MVD detector and also including the thickness of the aluminium window foils, and  $\sum_i k_i \cdot \Delta\theta_{\text{ms}}$  is the extrapolation error due to the multiple Coulomb scattering along the particle direction,  $\Delta\theta_{\text{ms}}^2 \propto p_{\text{beam}}^{-2}$  [29].

To extract the intrinsic position resolution of the MVD detector ( $\sigma_{\text{MVD}}^{\text{intr}}$ ), the contributions of the second (see subsection 2.1) and third term in equation 6 have been evaluated. The effect of the multiple Coulomb scattering at low beam energy (2-6 GeV) cannot be neglected; the intrinsic resolution has been extracted by fitting the residual distribution measured at several beam energies (shown in figure 9) to the formula in equation 6. Since the production of  $\delta$ -rays can spoil the position resolution, (see subsection 7.4), a selection cut to reject the events in the tail of the energy loss distribution has been applied in the previous calculation:

$$S_{\text{cluster}} \leq 1.7 \cdot S_{\text{peak}}$$

where  $S_{\text{cluster}}$  is the total cluster charge and  $S_{\text{peak}}$  is the most probable energy deposition. The intrinsic position resolution obtained for the MVD detector at  $\theta = 0^\circ$  incidence angle is:

$$\sigma_{\text{MVD}}^{\text{intr}} = 7.2 \pm 0.2 \mu\text{m}$$

Different strip lengths do not affect significantly neither the resolution nor the charge division mechanism [22].

### 5.3 Resolution vs interstrip hit position

Figure 10(a) shows the position resolution as a function of the interstrip hit position. The presence of an alternate systematic pattern when moving from a  $p^+$  implant to the next one is noticeable. However, the variations observed are in general very small ( $\lesssim 1\mu\text{m}$ ). In the region close to the readout strips, the position resolution becomes slightly worse. This effect is a consequence of the use of only two readout strips for the position reconstruction: when

a particle traverses the silicon sensor very close to a readout strip, a high signal is induced on that readout strip and only relatively small signals on the neighbouring ones. Therefore the  $\eta$  algorithm becomes more sensitive to noise fluctuations. Figure 10(b) shows the mean value of the Gaussian fit to the residual distribution (corresponding to a systematic shift from the origin) as a function of the interstrip hit position. Close to the readout strips the systematic shift in the position reconstruction is larger ( $\sim 1.5\text{-}2\ \mu\text{m}$ ) than in the central area between readout strips ( $\lesssim 1\ \mu\text{m}$ ).

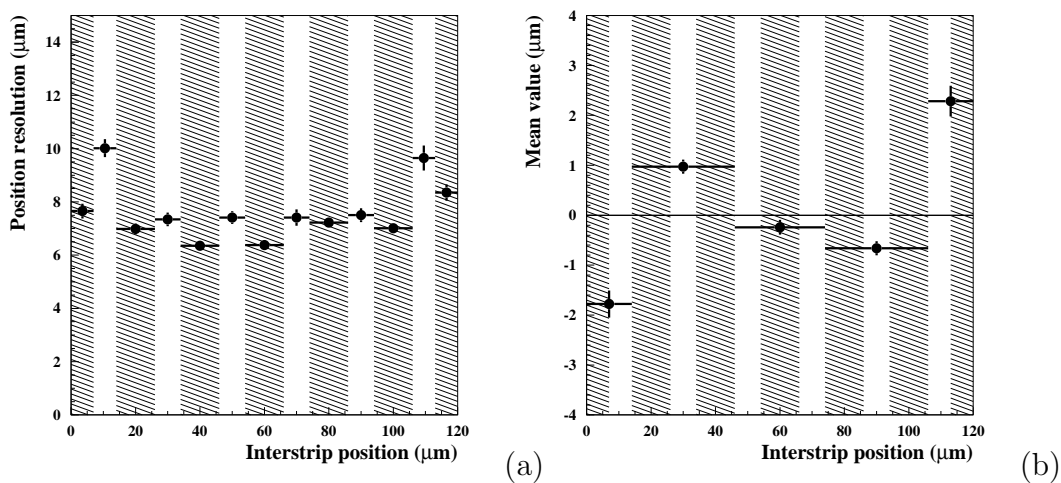


Fig. 10. (a) Position resolution and (b) average residual shift from the origin as a function of the interstrip hit position. Note that in this case no cut to reject  $\delta$ -electrons has been applied. The hatched bands indicate the position of the readout and intermediate strips.

## 6 Position reconstruction for small angle of incidence tracks

### 6.1 The 3-strips algorithm

The use of only two readout strips to extract position information may not be the most appropriate choice for the MVD detectors, since the symmetric charge sharing to the next-to-closest readout strips is not negligible. Figure 11 shows the cluster size distribution at four different incidence angles ( $0^\circ$ ,  $10^\circ$ ,  $20^\circ$ ,  $30^\circ$ ). At  $\theta = 0^\circ$ , already  $\sim 28\%$  of all cluster consists of more than two strips and this percentage becomes much larger ( $\gtrsim 45\%$ ) for  $\theta \gtrsim 20^\circ$ . An

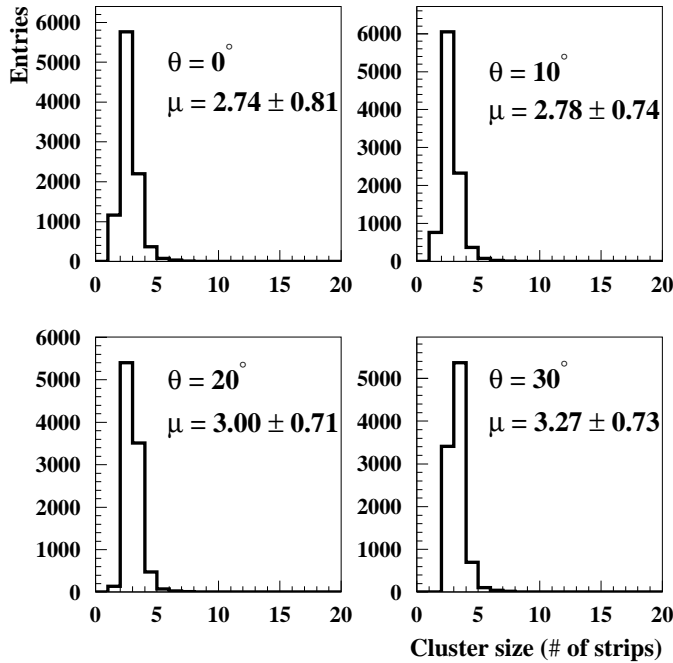


Fig. 11. Cluster size distribution for small incidence angles ( $0^\circ$ ,  $10^\circ$ ,  $20^\circ$ ,  $30^\circ$ ). The mean value and the rms of the cluster size distribution are also indicated.

alternative position reconstruction algorithm, which makes use of three strips, has been therefore developed. From each cluster, the strip with the highest signal,  $k$ , and its closest neighbours ( $k-1, k+1$ ) are selected and the following



quantities are calculated:

$$p_{\text{left}} = \frac{S_k \cdot k + S_{k-1} \cdot (k-1)}{S_k + S_{k-1}} \quad \text{and} \quad p_{\text{right}} = \frac{S_k \cdot k + S_{k+1} \cdot (k+1)}{S_k + S_{k+1}} \quad (7)$$

The uncorrected reconstructed position  $p_{\text{rec}}$  (in analogy to the linear  $\eta$  interpolation) is then defined as:

$$p_{\text{rec}} = \frac{p_{\text{left}} \cdot w^n + p_{\text{right}}}{1 + w^n} \quad \text{where} \quad w = S_{k-1}/S_{k+1}; \quad n = 2. \quad (8)$$

$n = 2$  is found to work better than  $n = 1$  because in the former case noise is suppressed by giving less weight to the strip with the lowest charge. The corresponding interstrip position  $\tilde{p}$  is given by:

$$\tilde{p} = \text{mod}(p_{\text{rec}}, 1.)$$

Figure 12 shows the  $dN/d\eta$  and  $dN/d\tilde{p}$  distributions for small incidence angles ( $0^\circ$ ,  $10^\circ$ ,  $20^\circ$ ,  $30^\circ$ ). By means of the 3-strips algorithm a more uniform distribution can be obtained. In analogy with the  $\eta$  algorithm a probability density function can be defined and the corrected impact position is given by:

$$y_{\text{rec}} = p \cdot f(\tilde{p}_0) + p \cdot p_{\text{left}} \quad (9)$$

where  $p$  is the readout pitch and  $p_{\text{left}}$  denotes the position reconstructed using the left and the central strips. Figure 13 shows the comparison between  $f(\tilde{p})$  and  $f(\eta)$  for  $\theta = 0^\circ$ . The position resolutions obtained using the  $\eta$  algorithm and the 3-strips algorithm for the four different incidence angles ( $0^\circ$ ,  $10^\circ$ ,  $20^\circ$ ,  $30^\circ$ ) are shown in figure 14. The resolution at  $0^\circ$  calculated with the 3-strips algorithm is slightly worse than the one obtained with the  $\eta$  algorithm. Nevertheless the non-linearity correction for the 3-strips algorithm is much smaller than the one needed for the  $\eta$  algorithm up to  $30^\circ$ , as shown in the right

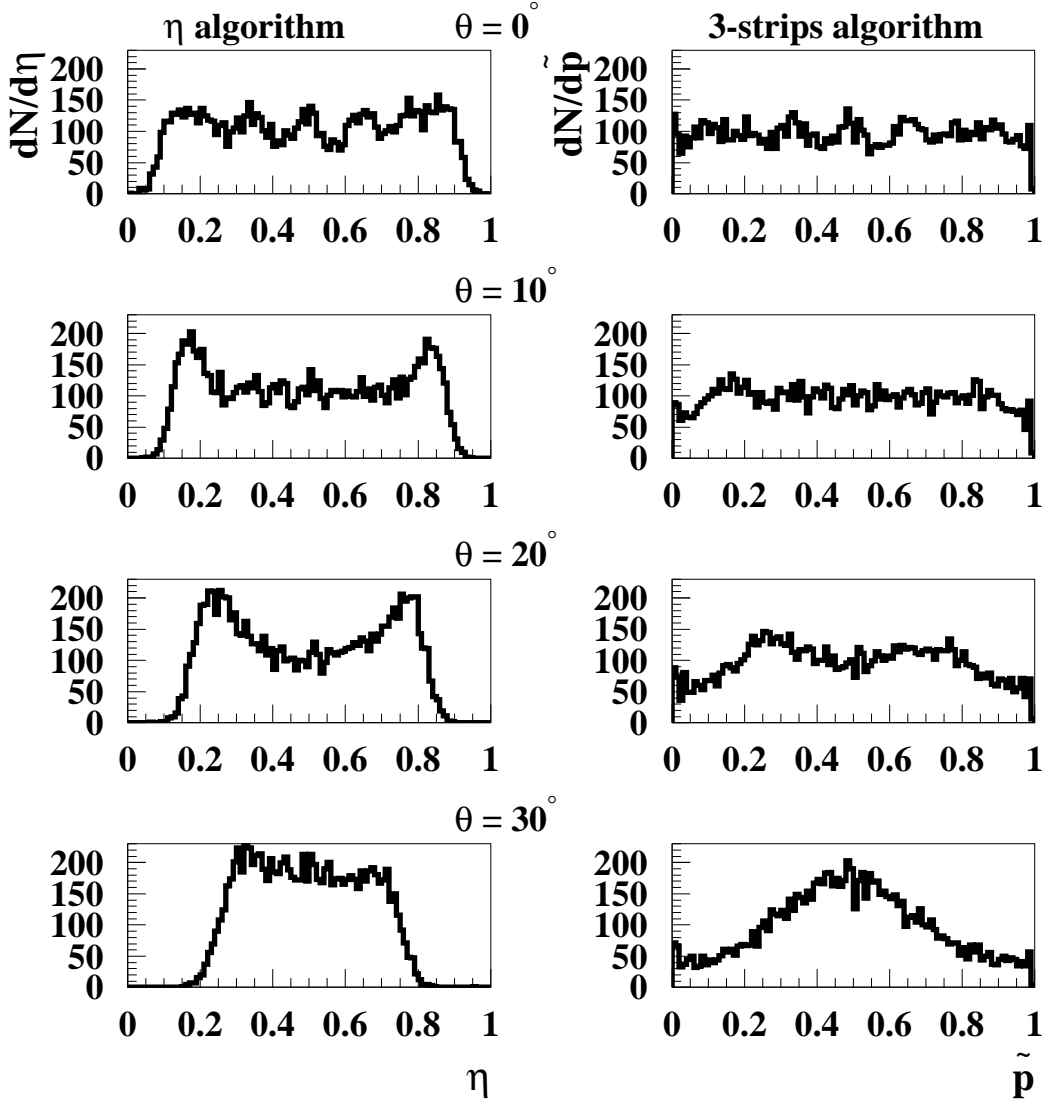


Fig. 12.  $dN/d\eta$  and  $dN/d\tilde{p}$  distributions for small incidence angles.

plot of figure 14. Thus the 3-strips algorithm is much less sensitive to possible variations in the probability density function due to non-uniformities of the MVD detectors. A simple centre of gravity algorithm has been discarded since its use results in a significantly worse position resolution for particle crossing the detector in the central region between two readout strips and in addition it introduces sizeable systematic shifts in the position reconstruction.

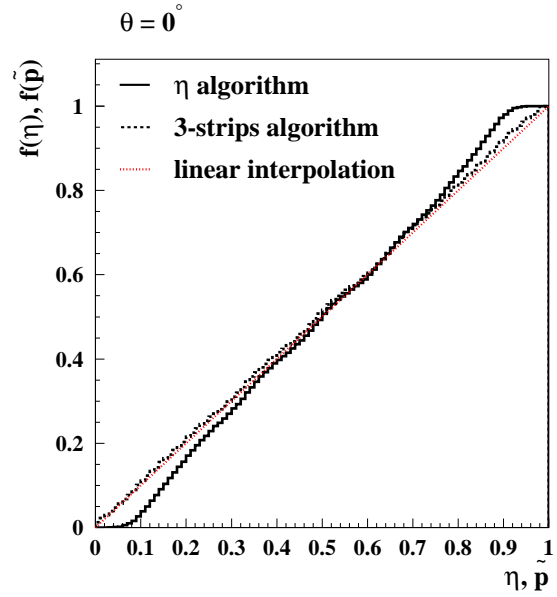


Fig. 13. Probability density function for the  $\eta$  and the 3-strips algorithm. Note that at  $\theta = 0^\circ$  the result for  $f(\tilde{p})$  is very close to the linear interpolation.

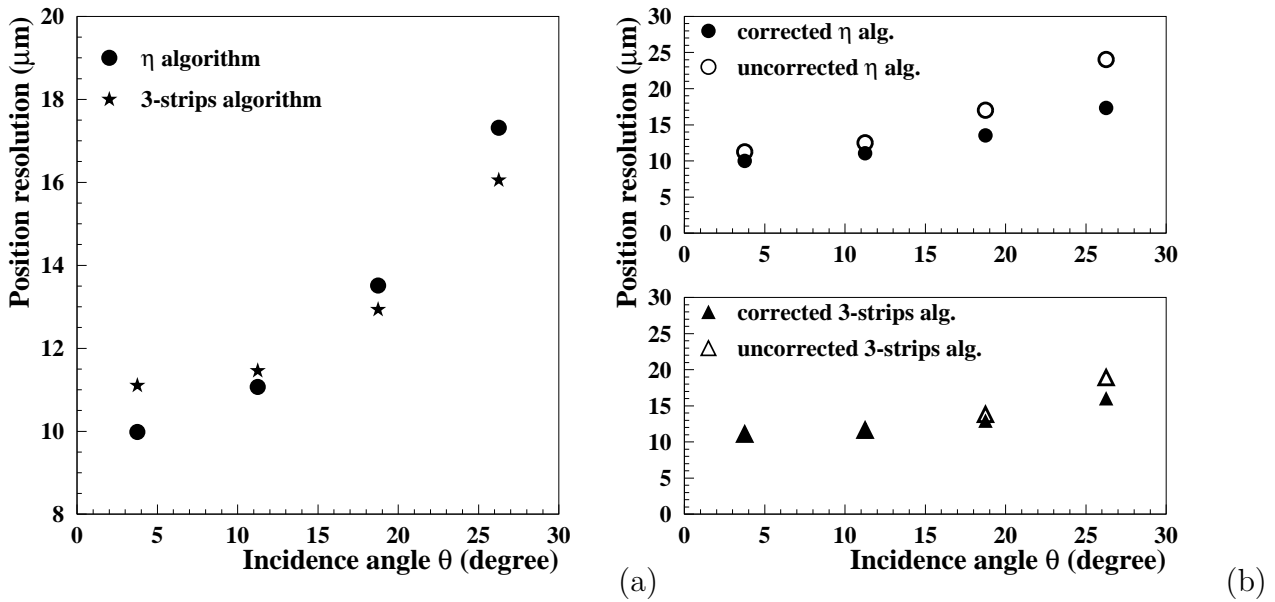


Fig. 14. Position resolution for small incidence angles ( $0^\circ$ ,  $10^\circ$ ,  $20^\circ$ ,  $30^\circ$ ). (a) Comparison between the corrected position resolution calculated using the  $\eta$  and the 3-strips algorithm; (b) comparison between the uncorrected and corrected position resolution for both algorithms.

## 6.2 Performance as a function of the $\phi$ angle

In the barrel section of the MVD the angle  $\phi$  can be as large as  $70^\circ$ . However the size of the optical bench in the testbeam setup limited the measurement to a maximum angle  $\phi$  of  $30^\circ$ . In the forward section of the MVD the  $\phi$  range is bigger than the  $\theta$  range due to the orientation and position of the FMVD strips with respect to the interaction point<sup>5</sup>. Although the maximum angle  $\phi$  in the FMVD is only  $\sim 30^\circ$ , this is correlated with physical quantities of interest such as the pseudorapidity of the track; any systematic effect could be thus relevant for high momentum tracks as the one of the scattered electron at high  $Q^2$ . In the data analysis for the FMVD sensors, the width of the residual distribution was  $\sim 2\text{-}3\ \mu\text{m}$  larger than in the standard setup (used for BMVD sensors) because of the different geometrical constraints (i.e. the telescope modules had to be moved away from the MVD sensor). The expected increase of the signal with the path length inside the detector ( $\propto \cos(\phi)^{-1}$ ) was observed [22].

Figure 15(a) shows the position resolution as a function of the angle  $\phi$  for several beam energies. A rather flat behaviour is observed in the relevant range for the FMVD. In figure 15(b) the squared position resolution as a function of  $1/E^2$  is shown for two different angles ( $0^\circ$  and  $30^\circ$ ). The contribution of multiple scattering shows up as a linear behaviour and the intrinsic resolution corresponds to the intercept at the origin (i.e. for infinite momentum particles) as it was discussed in subsection 5.2. The data at  $\phi = 30^\circ$  (squares) seem to have a larger slope and a smaller intercept compared with the results for  $\phi = 0^\circ$  (dots). The larger slope can be attributed to the increase in the material of

---

<sup>5</sup> This is true if the curvature induced by the magnetic field is not taken into account. For low momenta particles the angle  $\theta$  can be also large.

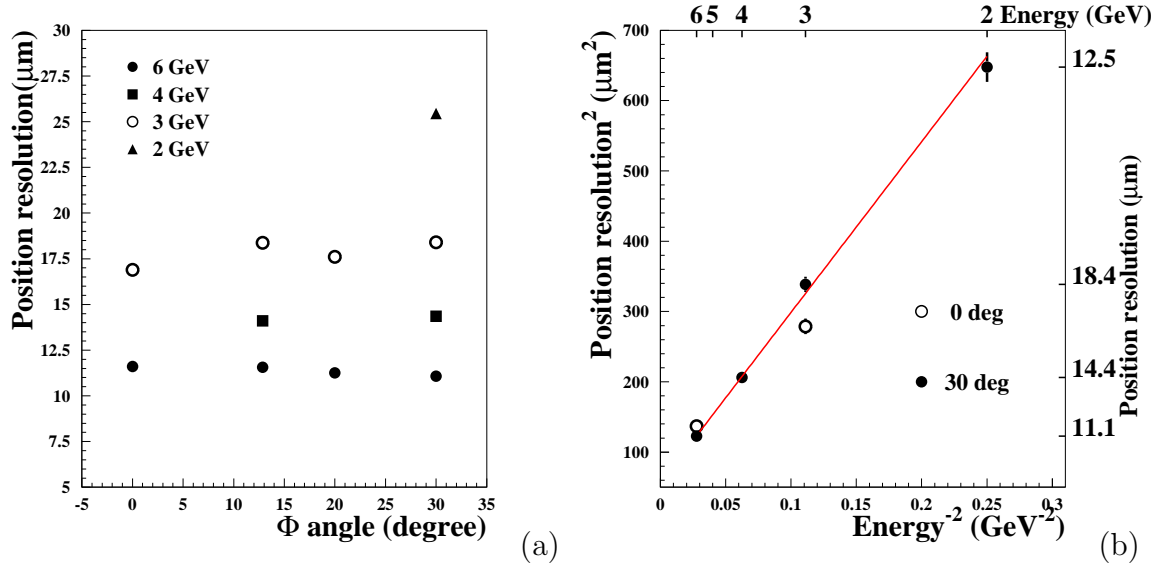


Fig. 15. (a) Position resolution as a function of the angle  $\phi$ ; (b)  $\sigma^2$  as a function of  $1/E^2$ . A fit to the data at  $\phi = 30^\circ$  is also shown.

a factor  $\cos(30^\circ)^{-1} \sim 1.15$ . In addition, the larger S/N obtained at larger  $\phi$  angles can produce a better intrinsic resolution (as indicated by the smaller intercept). Systematic effects have been evaluated to be smaller than 4%, dominating over the statistical accuracy of  $\sim 1.4\%$ .

## 7 Position resolution for large angle of incidence tracks

At large incidence angles ( $\theta > 30^\circ$ ) the charge is spread over several strips and the total cluster signal becomes larger as the particle's path length increases:

$$S(\theta) \propto \frac{S(\theta = 0^\circ)}{\cos \theta} \quad (10)$$

Since the central strips have on average the same signal, the information on

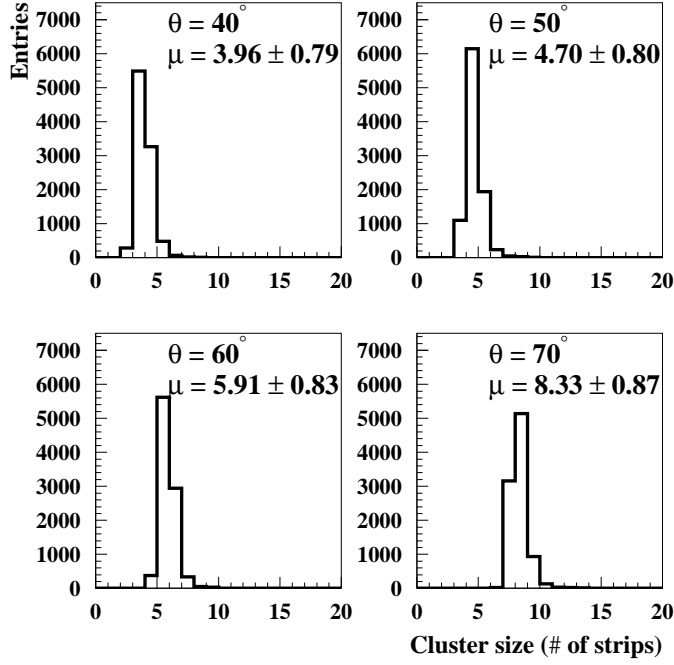


Fig. 16. Cluster size distributions for large incidence angles ( $40^\circ$ ,  $50^\circ$ ,  $60^\circ$ ,  $70^\circ$ ) the impact position is essentially contained only in the positions and signals of the cluster edge strips. Therefore reconstruction algorithms such as the  $\eta$  one are inadequate to calculate the particle impact point on the detector. Figure 16 shows the cluster size distributions for large angles of incidence ( $40^\circ$ ,  $50^\circ$ ,  $60^\circ$ ,  $70^\circ$ ). Figure 17(a) shows the energy loss distribution for various incidence angles ( $0^\circ$ ,  $30^\circ$ ,  $50^\circ$ ,  $60^\circ$ ,  $70^\circ$ ), whereas the most probable value for the energy deposition as a function of the incidence angle is shown in figure 17(b). In this case the energy deposition is defined by summing up the signals measured on  $\pm 5$  strips around the predicted position:

$$S_{\text{tot}} = \sum_{i=-5}^{+5} S_i$$

The result of a fit to the function:

$$f(\theta, P_1, P_2) = \frac{P_1}{\cos \theta P_2} \tag{11}$$

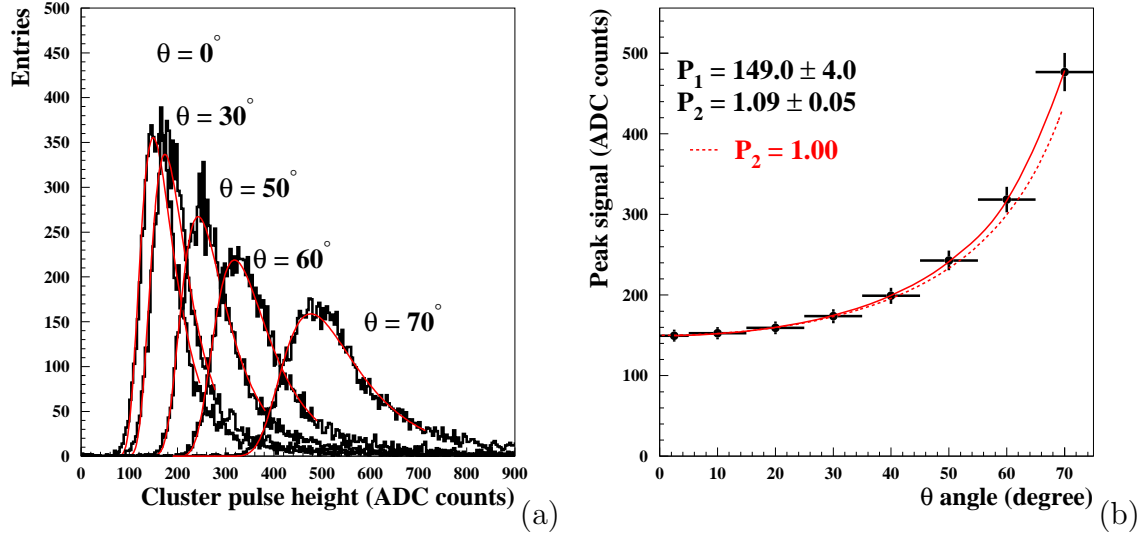


Fig. 17. (a) Energy loss distribution at various incidence angles; (b) most probable value for the energy deposition as a function of the incidence angle.

is also presented. The value  $P_2 = 1.09 \pm 0.05$  is in agreement with the expectation in equation 10 (i.e.  $P_2 = 1.0$ ).

### 7.1 The head-tail algorithm

A standard position reconstruction algorithm, proven to work at large incidence angle, is the so called ‘head-tail’ algorithm [28, 30]. All the strips with:

$$S_{\text{strip}} > 3 \cdot \sigma_{\text{chip}}$$

where  $S_{\text{strip}}$  is the strip signal and  $\sigma_{\text{chip}}$  is the average chip noise, are considered. The first (head) and the last (tail) strips belonging to a cluster are selected and the impact position is defined as:

$$y_{\text{rec}} = \frac{y_{\text{head}} + y_{\text{tail}}}{2} + \text{ht}_{\text{corr}} \quad \text{with} \quad \text{ht}_{\text{corr}} = \frac{S_{\text{tail}} - S_{\text{head}}}{2 \cdot \langle S \rangle_{\text{strips}}} \cdot p \quad (12)$$

where  $y_{\text{head}}$  ( $y_{\text{tail}}$ ) is the position of the head (tail) strip,  $S_{\text{head}}$  ( $S_{\text{tail}}$ ) is the corresponding signal,  $p$  is the strip pitch and  $\langle S \rangle$  is the average strip signal over the cluster.

The difference ( $S_{\text{tail}} - S_{\text{head}}$ ) in the correction factor  $ht_{\text{corr}}$  is used to shift the average position  $(y_{\text{head}} + y_{\text{tail}})/2$  towards the tail ( $S_{\text{tail}} - S_{\text{head}} > 0$ ) or head ( $S_{\text{tail}} - S_{\text{head}} < 0$ ) strip of the cluster, taking into account the rough proportionality of the energy loss to the particle path in the detector.

## 7.2 Comparison with the simulation

Figure 18 shows the position resolution calculated with the  $\eta$  and head-tail algorithms as a function of the angle of incidence  $\theta$ . At angles  $\lesssim 30^\circ$  the  $\eta$  algorithm gives a much better resolution than the head-tail algorithm. However for angles  $\gtrsim 30\text{-}40^\circ$ , the latter proves to work much better. The results using two different MVD barrel detectors are presented and compared with the results obtained using the simulation program. The simulation is able to describe the data over the whole angular region and for both reconstruction algorithms. The S/N and charge transfer coefficients of det. #1 were used in the simulation, which explains the slightly better agreement with this detector. Since  $\delta$ -rays (see next section) are not taken into account the simulated intrinsic resolution is found to be better than the one obtained from testbeam data, especially for the  $\eta$  algorithm at small incident angles. The probability that the two highest strips in the cluster, i.e. those used by the  $\eta$  algorithm, are affected by a  $\delta$ -ray which departs from the initial trajectory is smaller at larger angles because the energy is deposited along more strips.



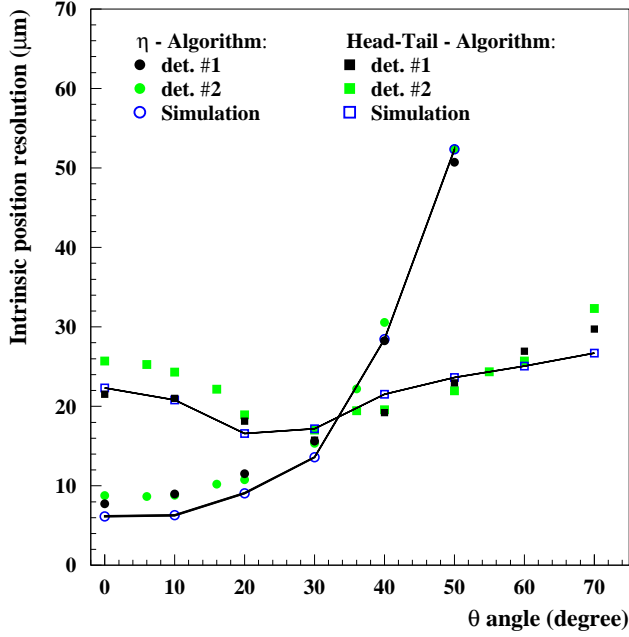


Fig. 18. Intrinsic position resolution calculated with the  $\eta$  and head-tail algorithms as a function of the angle of incidence  $\theta$ .

### 7.3 Optimisation of the reconstruction algorithm

Reconstruction algorithms such as the  $\eta$ , 3-strips or the head-tail ones are based on the knowledge of the incidence angle  $\theta$  of the particle, used to select the most effective algorithm to be applied. Switching between different reconstruction algorithms clearly implies complications in the track reconstruction procedure. Ideally an optimal algorithm should calculate impact positions with a single calculation procedure, using as little additional external information as possible to minimise systematic effects.

A first simple attempt for a more general algorithm can be based only on the rough knowledge of the angle  $\theta$  of the incident particle at which the switch between two different algorithms is required ( $\theta_{\text{cut}}$  algorithm):

- if  $\theta \lesssim \theta_{\text{cut}}$  (with  $\theta_{\text{cut}} \simeq 30\text{-}40^\circ$ ) the uncorrected 3-strips algorithm is used

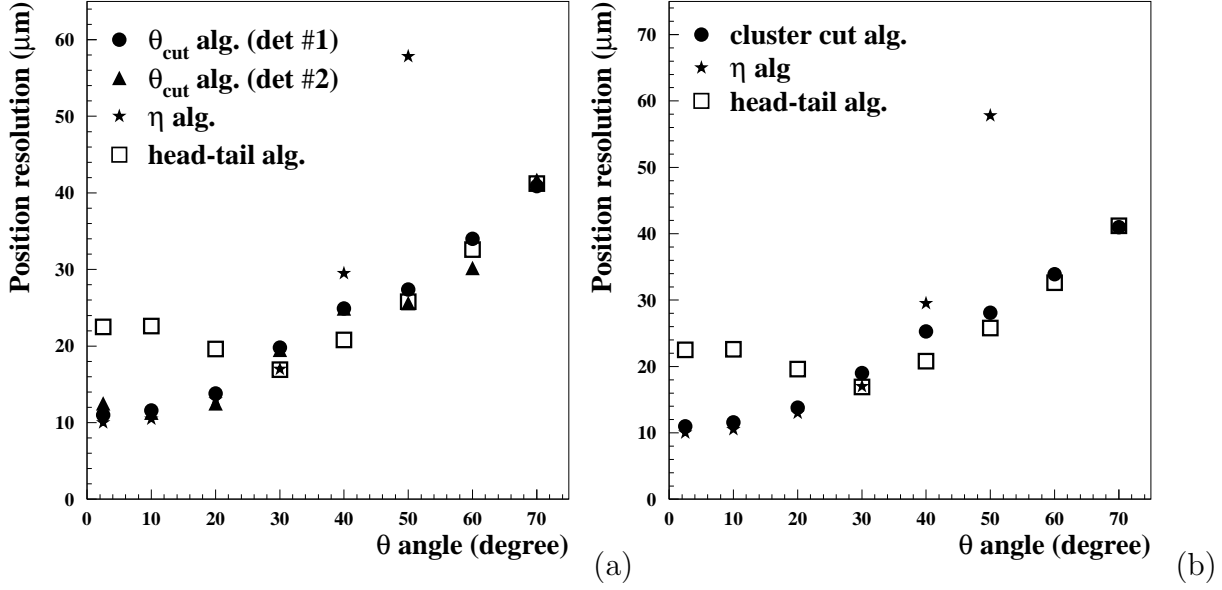


Fig. 19. Position resolution as a function of the angle of incidence  $\theta$  calculated using (a) the  $\theta_{\text{cut}}$  reconstruction algorithm (b) the cluster-cut algorithm. The comparison with the  $\eta$  and head-tail algorithm is also shown.

- if  $\theta > \theta_{\text{cut}}$  the head-tail algorithm is used.

Since the non-linearity correction is not applied, a slightly worse position resolution at small angles is obtained. Figure 19(a) shows the position resolution obtained with this algorithm as function of the incidence angle  $\theta$  for two different detectors.

A more general algorithm based on the use of the cluster size,  $N_{\text{strips}}$  and a cluster shape parameter,  $R_{\text{out}}$ , is presented in this paper. The ‘cluster cut’ algorithm uses two different calculations as detailed in the following:

- if  $N_{\text{strips}} < N_{\text{cut}}$  and  $R_{\text{out}} < R_{\text{cut}}$ , where  $R_{\text{out}} = (S_{k-2} + S_{k+2})/S_k$ , the 3-strips algorithm is used.
- if  $N_{\text{strips}} > N_{\text{cut}}$  or  $R_{\text{out}} \geq R_{\text{cut}}$  the head-tail algorithm is employed.

To a good approximation the cluster size is directly correlated to the angle

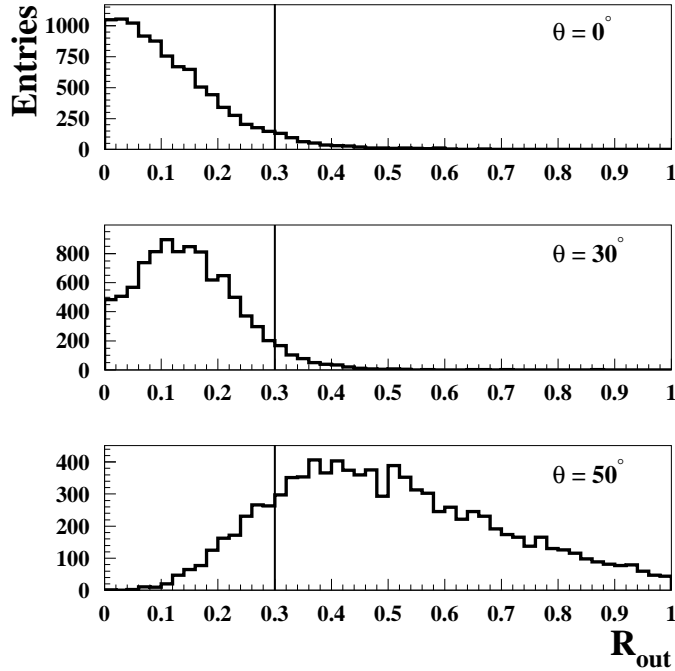


Fig. 20.  $R_{\text{out}}$  distribution at  $\theta = 0^\circ$ ,  $30^\circ$ ,  $50^\circ$ .

of incidence, i.e. small clusters ( $N_{\text{strips}} \sim 2-3$ ) are most likely originated by tracks crossing the detector at small angles of incidence whereas large clusters ( $N_{\text{strips}} > 6$ ) are due to particles crossing the detector at large angles of incidence. For intermediate cluster sizes, a matching ambiguity remains. However, the cluster shape also depends on the angle of incidence: for larger angles, the track path length is relatively large and thus also the outer strips of smaller clusters have a sizable signal (compared to the highest signal in the cluster). By making use of this additional information, the ambiguity can be reduced. The values  $R_{\text{cut}}=0.3$  and  $N_{\text{strips}}=5$  (same results are obtained for  $N_{\text{strips}}=6$ ) have been used in this analysis. The cut value for  $R_{\text{cut}}$  has been chosen by comparing the distribution for different incidence angles (see figure 20).

Figure 19(b) shows the comparison between the position resolution obtained with the 'cluster cut' algorithm and the position resolution obtained with

the  $\eta$  and the head-tail algorithms. The position resolution achieved with the uncorrected ‘cluster-cut’ algorithm is only slightly worse than the one calculated with the best standard reconstruction method for each angle (i.e.  $\eta$  and ‘head-tail’). Since the ‘cluster-cut’ algorithm does not need any angular information, it could be a valuable choice for a first position reconstruction in a general track reconstruction procedure.

#### *7.4 Impact of $\delta$ -rays on the position resolution*

The production of  $\delta$ -rays (i.e. knock-on electrons), responsible for the tail in the energy loss distribution, influences the detector resolution, as it affects the deposited charge distribution in the silicon bulk. The  $\delta$ -ray trajectory results in deposition of charge off the incident particle’s path and therefore displaces the charge centre of gravity. The position resolution for larger pulse height becomes significantly worse as can be seen in Figure 21, where the width of the residual distribution as a function of the cluster pulse height for incident angles between  $0^\circ$  and  $70^\circ$  is shown. The hit position is reconstructed using the  $\eta$ -algorithm up to angles of incidence of  $30^\circ$ , whereas for larger incident angles the head-tail algorithm is used. Although the resolution is worse, events with large signal cluster cannot be excluded in the tracking reconstruction for the MVD, because the loss in reconstruction efficiency would be too high. However, it is possible to assign different weights to the reconstructed hits when performing the track fit.

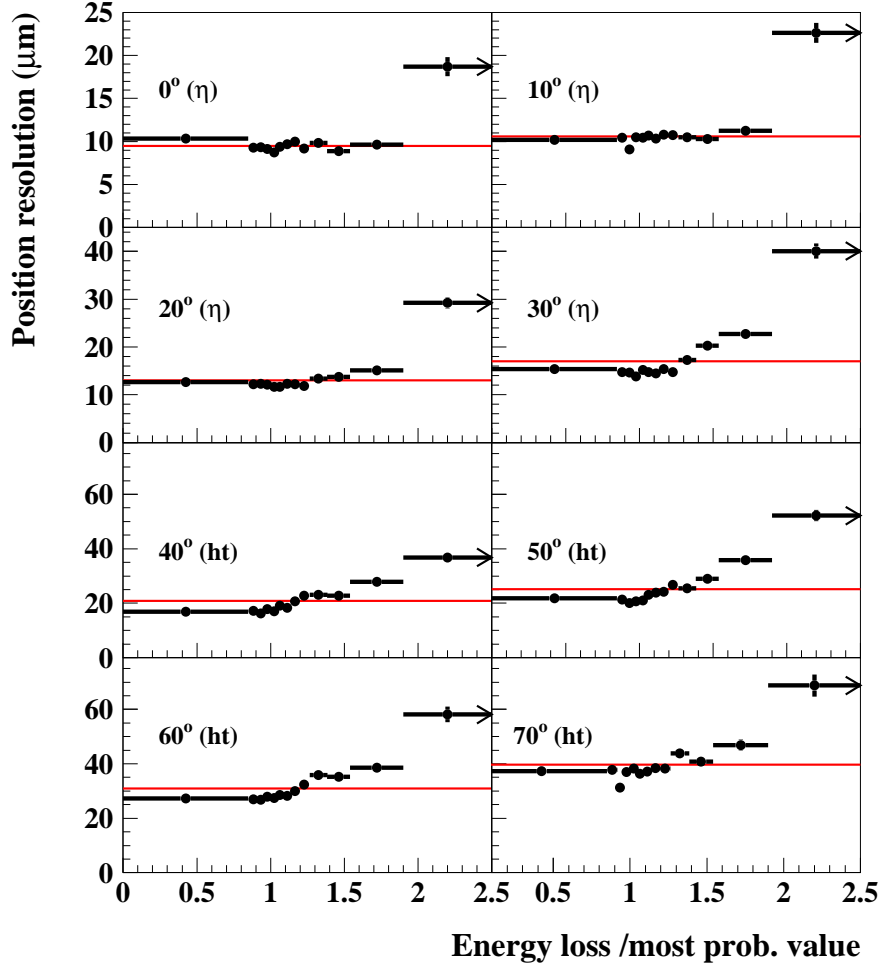


Fig. 21. Position resolution as a function of the energy loss for incident angles between  $0^\circ$  and  $70^\circ$ . The line indicates the average position resolution.

## 8 Summary of the results

The testbeam setup at DESY has been used to characterise the performance of BMVD and FMVD detectors plus the prototype readout electronics (HELIX chips). The main results from the testbeam measurements presented in this paper can be summarised as follows:

- a signal over noise ratio  $S/N \simeq 20-24$  has been achieved, the noise level is

uniformly distributed over the strips;

- the detector efficiency  $\epsilon$  is very high ( $> 99.95\%$ );
- the calibration shows that gain variations of a single HELIX readout chip are of the order of 2% and do not influence the position reconstruction algorithm even in the case of detectors with strips of different lengths (FMVD);
- the charge division has been studied in detail. The expected charge sharing between strip implants has been confirmed;
- the charge transfer between strip implants and readout strips has been parameterised and implemented in a detector simulation program which gives a good description of the data;
- the intrinsic position resolution at normal angle of incidence  $\sigma_{\text{MVD}}^{\text{intr}} = 7.2 \pm 0.2 \mu\text{m}$  is highly satisfactory if compared to the value  $p/\sqrt{12} \simeq 35 \mu\text{m}$  which represents the limit for a digital system with a readout pitch  $p = 120 \mu\text{m}$ ;
- the position resolution is not strongly dependent on the angle  $\phi$  in the range of interest for the FMVD;
- the position resolution at large angle of incidence  $\theta$  is still very satisfactory ( $\lesssim 40 \mu\text{m}$  up to  $\theta = 70^\circ$ );
- a position reconstruction algorithm which uses the rough knowledge of the angle of incidence  $\theta$  to choose the most effective reconstruction procedure has been developed. For small incidence angles a 3-strips algorithm is applied whereas for large incidence angles the head-tail algorithm is used;
- a general position reconstruction algorithm, not using prior knowledge of the angle of incidence, has proven to work well up to  $\theta = 70^\circ$  and could therefore be a valuable choice for a first position reconstruction in the track reconstruction procedure;
- the production of  $\delta$ -rays causes a deterioration of the position resolution. Since events with very large cluster signal cannot be excluded from the MVD data, the hit positions used for a track fit should be weighted according to

their pulse height.

## References

- [1] U. Schneekloth (editor), “The HERA Luminosity Upgrade”, DESY internal report, DESY-HERA 98-05, 1998.
- [2] ZEUS Collaboration, M. Derrick et al., The ZEUS Detector, Status Report 1993, DESY, 1993.
- [3] A. Garfagnini, *Nucl. Instrum. Methods A* **435**, 1999 (34).
- [4] R. Klanner, “The ZEUS Micro Vertex Detector”, proceedings of the International Europhysics Conference on High Energy Physics, EPS-HEP 99, Tampere, Finland.
- [5] E. Koffeman, *Nucl. Instrum. Methods A* **453**, 2000 (89).
- [6] C. Coldewey, *Nucl. Instrum. Methods A* **453**, 2000 (149).
- [7] M. Feuerstack-Raible, U. Trunk, et al, “HELIX 128-x User’s Manual Version 2.1, 3.2.1999 ”, HD-ASIC-33-0697. Available at <http://wwwasic.kip.uni-heidelberg.de/~trunk/projects/Helix/>.
- [8] M. Feuerstack-Raible, *Nucl. Instrum. Methods A* **447**, 2000 (35).
- [9] M. C. Petrucci, *Int. J. Mod. Phys. A* Vol. 16 Suppl. 1C (2001) 1078,
- [10] E. Koffeman, *Nucl. Instrum. Methods A* **473**, 2001 (26).
- [11] V. Chiochia, “The ZEUS Micro Vertex Detector”, proceedings of the Vertex 2002 conference, hep-ex/0111061, submitted to *Nucl. Instrum. Methods A*.
- [12] C. Coldewey, *Nucl. Instrum. Methods A* **447**, 2000 (44).
- [13] A. Garfagnini and U. Kötz, *Nucl. Instrum. Methods A* **461**, 2001 (158).

- [14] D. Dannheim et al., *Design and Tests of the Silicon Sensors for the ZEUS Micro Vertex Detector*, submitted for publication to *Nucl. Instrum. Methods A*.
- [15] U. Kötz, *Nucl. Instrum. Methods A* **461**, 2000 (210).
- [16] LabView, product of National Instruments.
- [17] C. Colledani et al., *Nucl. Instrum. Methods A* **372**, 1996 (379).
- [18] J. Straver et al., *Nucl. Instrum. Methods A* **348**, 1994 (485).
- [19] M. Milite, PhD Thesis, DESY-THESIS-2001-050. Available at <http://www-library.desy.de/cgi-bin/showprep.pl?desy-thesis-01-050>.
- [20] ICI Films, High Performance Films Group, Wilmington, Delaware 19897, USA.
- [21] CERN EST/SM-CI, Photomechanical Technologies Workshop.
- [22] I. Redondo, PhD Thesis, DESY-THESIS-2001-037. Available at <http://www-library.desy.de/cgi-bin/showprep.pl?desy-thesis-01-037>.
- [23] Internal communication on test of the F/E chips (unpublished). Available at <http://zeus.pd.infn.it/MVD/MVD.html>.
- [24] M. Moritz, PhD Thesis, DESY-THESIS-2002-009. Available at <http://www-library.desy.de/cgi-bin/showprep.pl?desy-thesis-02-009>
- [25] G. Bashindzhagyan and N. Korotkova, *Simulation of Silicon Microstrip Detector Resolution for ZEUS Vertex Upgrade*, internal ZEUS note, 99-023, Hamburg (Germany), (1999).
- [26] J. Martens, *Simulationen und Qualitätssicherung der Siliziumstreifendetektoren des ZEUS-Mikrovertexdetektors*, DESY-THESIS-1999-044, Diplomarbeit, University of Hamburg (1999).
- [27] E. Belau et al., *Nucl. Instrum. Methods* **214**, 1983 (253).



- [28] R. Turchetta, *Nucl. Instrum. Methods A* **335**, 1993 (44).
- [29] D.E. Groom et al., *The European Physical Journal C*15 (2000) 1.
- [30] KEK Preprint 96-172, *Measurement of the Spatial Resolution of Wide-pitch Silicon Strip Detectors with Large Incident Angle*.